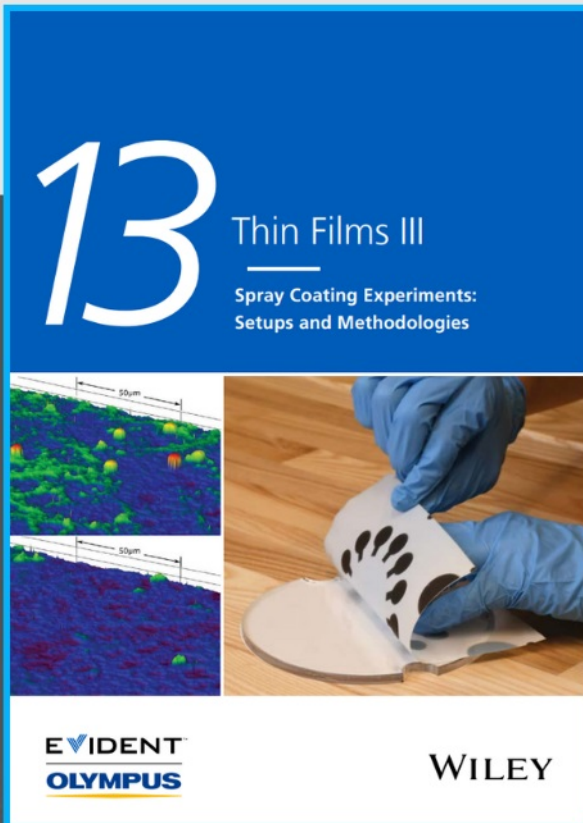




Spray Coating Experiments: Setups and Methodologies



**The latest eBook from
Advanced Optical Metrology.
Download for free.**

Spray Coating Experiments: Setups and Methodologies, is the third in our Thin Films eBook series. This publication provides an introduction to spray coating, three article digests from Wiley Online Library and the latest news about Evident's Image of the Year Award 2022.

Wiley in collaboration with Evident, are committed to bridging the gap between fundamental research and industrial applications in the field of optical metrology. We strive to do this by collecting and organizing existing information, making it more accessible and useful for researchers and practitioners alike.

EVIDENT
OLYMPUS

WILEY

Engineering Periodic Dinuclear Lanthanide-Directed Networks Featuring Tunable Energy Level Alignment and Magnetic Anisotropy by Metal Exchange

Daniel Moreno, Sofia O. Parreiras,* José I. Urgel, Beatriz Muñoz-Cano, Cristina Martín-Fuentes, Koen Lauwaet, Manuel Valvidares, Miguel A. Valbuena, José M. Gallego, José I. Martínez, Pierluigi Gargiani, Julio Camarero, Rodolfo Miranda, and David Écija*

The design of lanthanide multinuclear networks is an emerging field of research due to the potential of such materials for nanomagnetism, spintronics, and quantum information. Therefore, controlling their electronic and magnetic properties is of paramount importance to tailor the envisioned functionalities. In this work, a multidisciplinary study is presented combining scanning tunneling microscopy, scanning tunneling spectroscopy, X-ray absorption spectroscopy, X-ray linear dichroism, X-ray magnetic circular dichroism, density functional theory, and multiplet calculations, about the supramolecular assembly, electronic and magnetic properties of periodic dinuclear 2D networks based on lanthanide-pyridyl interactions on Au(111). Er- and Dy-directed assemblies feature identical structural architectures stabilized by metal–organic coordination. Notably, despite exhibiting the same +3 oxidation state, there is a shift of the energy level alignment of the unoccupied molecular orbitals between Er- and Dy-directed networks. In addition, there is a reorientation of the easy axis of magnetization and an increment of the magnetic anisotropy when the metallic center is changed from Er to Dy. Thus, the results show that it is feasible to tune the energy level alignment and magnetic anisotropy of a lanthanide-based metal-organic architecture by metal exchange, while preserving the network design.

and emerging science and technology for photonics, energy conversion, telecommunications, sensing, catalysis, magnetism, superconductivity, biomedicine, and quantum engineering.^[1–11]


In this regard, single-molecule magnets (SMMs) based on lanthanides have been intensively studied in the last few years aiming the stabilization of magnetic moments at the molecular level and the development of higher density storage applications.^[5,12–19] The slow relaxation times, high magnetic moments, and bistable ground state of lanthanides make them very suitable for molecular spintronic applications.^[5,12,13] A logical extension of the lanthanide-driven SMM approach would be the engineering of periodic networks containing lanthanides, which could act as the active magnetic information units.

In the past decades, metallosupramolecular protocols have emerged as a powerful strategy to engineer functional reticular materials embedding metal elements.^[20–22] Such synthetic paradigm has also been developed on surfaces, being able to engineer 2D metal–organic designs, mostly employing transition and alkali metals.^[23–25]

1. Introduction

The physics and chemistry of lanthanides are receiving nowadays widespread attention due to their relevance in modern

D. Moreno, S. O. Parreiras, J. I. Urgel, B. Muñoz-Cano, C. Martín-Fuentes, K. Lauwaet, M. A. Valbuena, J. M. Gallego, J. Camarero, R. Miranda, D. Écija
Instituto Madrileño de Estudios Avanzados en Nanociencia (IMDEA Nanoscience)
Madrid 28049, Spain
E-mail: sofia.oliveira@imdea.org; david.ecija@imdea.org

 The ORCID identification number(s) for the author(s) of this article can be found under <https://doi.org/10.1002/smll.202107073>.

© 2022 The Authors. Small published by Wiley-VCH GmbH. This is an open access article under the terms of the Creative Commons Attribution-NonCommercial License, which permits use, distribution and reproduction in any medium, provided the original work is properly cited and is not used for commercial purposes.

M. Valvidares, P. Gargiani
ALBA Synchrotron Light Source
Cerdanyola del Vallès 08290, Spain

J. M. Gallego, J. I. Martínez
Instituto de Ciencia de Materiales de Madrid (ICMM-CSIC)
Cantoblanco, Madrid 28049, Spain

J. Camarero, R. Miranda
Departamento de Física de la Materia Condensada and Condensed Matter Physics Center (IFIMAC)
Universidad Autónoma de Madrid
Cantoblanco, Madrid 28049, Spain

DOI: 10.1002/smll.202107073

Despite the functional properties of lanthanides, which arise from the localized character of f-electrons, big atomic size, and inherent high spin-orbit coupling, only in the past decade the synthesis of lanthanide-directed coordinative architectures have been developed on surfaces.^[26–34] Notably, due to the inner character of f-electrons, metal-organic interactions therein are based on a dominant ionic character with a partial covalent character.^[1] As a result, the lanthanide coordinative sphere maximizes the coordination number, only limited by the steric interactions imposed by the ligand design. In fact, by a careful ex-professo synthesis of molecular building blocks and selection of functional groups, distinct lanthanide 2D nanoarchitectures comprising mononuclear coordination motifs could be achieved on surfaces. Only recently, non-periodic dinuclear Dy nanomeshes^[28,30] on Cu(111) and periodic Au/Ce heteronuclear networks on Au(111) could be achieved.^[35] In addition, the study of the electronic and magnetic properties of lanthanide-directed coordinative architectures is at its infancy and limited to mononuclear designs. Thus, it is crucial for the development of the field to design all-lanthanide multinuclear periodic metal-organic architectures on surfaces, in order to inspect their structures as well as their electronic and magnetic properties derived from their multinuclear character.

Here, we introduce lanthanide-directed dinuclear metal-organic architectures synthesized on a coinage metal, which are inspected and rationalized by a multidisciplinary study combining scanning tunneling microscopy (STM), scanning tunneling spectroscopy (STS), X-ray absorption spectroscopy (XAS), X-ray linear dichroism (XLD), X-ray magnetic circular dichroism (XMCD), density functional theory (DFT), and multiplet calculations. The sublimation of ditopic linear species equipped with terminal pyridyl functional groups on Au(111) followed by deposition of Er or Dy at convenient stoichiometries allows the design of rhombic or Kagome networks. Both lanthanides direct the same atomistic nanoarchitectures at a selected stoichiometry and coverage, which are based on dinuclear nodes. The inspection of their electronic properties by XAS, complemented by multiplet calculations, reveals a +3 oxidation state for both metal centers. STS measurements show a shift of the energy level alignment of the unoccupied orbitals between the structurally identical Er- and Dy-directed networks. Regarding the magnetic properties, inspected by XMCD, we show that Er-directed networks feature a tilted anisotropy axis, whereas Dy-directed architectures exhibit an in-plane anisotropy, which arises from the distinct distribution of the charge of the lanthanide center and the concomitant stabilization of the magnetic moment. Remarkably, the magnetic anisotropy of Dy is 2.6 times higher than Er.

Thus, we demonstrate the feasibility of engineering the magnetic anisotropy of lanthanide-directed dinuclear networks, as well as the energy level alignment, by metal exchange, while preserving the atomistic metal-organic coordination.

Our results open perspectives for the design of periodic multinuclear lanthanide-directed 2D materials, anticipating fascinating avenues for tailoring the electronic properties and magnetic anisotropy of the nanomaterials and, consequently, the envisioned optoelectronic and magnetic functionalities for applications in molecular optoelectronics, spintronics, and quantum technology.

2. Results and Discussion

The deposition of species [1,4-bis(4-pyridyl)-biphenyl] (DPBP) on Au(111) and subsequent annealing to 425 K gives rise to disordered reticular architectures based on Au-pyridyl coordinative interactions and N–H bonds between pyridyl functional groups and hydrogen of adjacent molecular species (Figure S1, Supporting Information).

This scenario drastically changes with the addition of a lanthanide element to the sample. As illustrated in **Figure 1a,b**, the deposition of Er or Dy on a close to monolayer coverage (the surface fully covered by the network) of DPBP at 1:1 lanthanide:ligand stoichiometry, and subsequent annealing to 425 K, results in the formation of rhombic-like porous architectures spanning hundreds of nanometers (see Figure S2, Supporting Information). Within each supramolecular domain, there is a minority of molecular species (<10%) featuring an offset of approximately 5° with respect to the major molecular orientation, thus allowing supramolecular flexibility. Importantly, our experiments did not show any difference between the rhombic Er- or Dy-DPBP metallosupramolecular networks, and, thus, both architectures are structurally identical and feature the same orientation (and probably registry) with respect to the substrate.

High resolution microscopy with a CO-functionalized tip reveals that the nodes are dinuclear (see Figure 1c). The Er–Er and Dy–Dy intermetal distances are (2.9 ± 0.5) Å. As a result, the Er–N and Dy–N distance (between the metal and the pyridyl group) is (2.4 ± 0.5) Å. At this point, it is worth pointing out that the Er⁺³ and Dy⁺³ ionic radii are very similar (see below for determination of the oxidation state), which justifies the identical network structure, as probed by STM. Such experimental internodal distances are in good agreement with our DFT calculations, which are 3.6 Å for Er–Er and 3.4 Å for Dy–Dy, respectively (Figure 1a–c; Figure S3, Supporting Information).

In addition, our high-resolution images also reveal that the aryl constituents feature a dihedral rotation to minimize steric hindrance, as previously seen for related species on surfaces.^[36] The DFT-optimized structures for the rhombic networks exhibit dihedral rotation angles of $\approx 32^\circ$ and 44° for the central and terminal rings, respectively, independently for the Er- or Dy- networks. Thus, the DFT structural characterization matches very well with experiments and provides very similar structures for both Er- and Dy- networks. Furthermore, as illustrated in Figure S3 (Supporting Information), the calculations reveal a buckling of 0.6 Å of two substrate atoms beneath the dinuclear node, which inter-atomic helps to stabilize the supramolecular assembly.

Importantly, by maintaining a 1:1 lanthanide:ligand stoichiometry, but halving the amount of deposited molecular species and lanthanide atoms, i.e., reducing the supramolecular pressure, a lanthanide-directed Kagome network could be achieved for both Er and Dy (see Figure 1d–f). Again, no significant differences in structure are found while employing the distinct lanthanides. High-resolution images acquired with a CO-functionalized tip reveal that the Kagome networks are based on Er/Dy dinuclear nodes, featuring three distinct orientations with respect to the substrate. Statistical analysis of the networks shows Er–Er and Dy–Dy distances of (3.3 ± 0.5) Å, resulting in Er–N and Dy–N projected distances of (2.4 ± 0.5) Å.

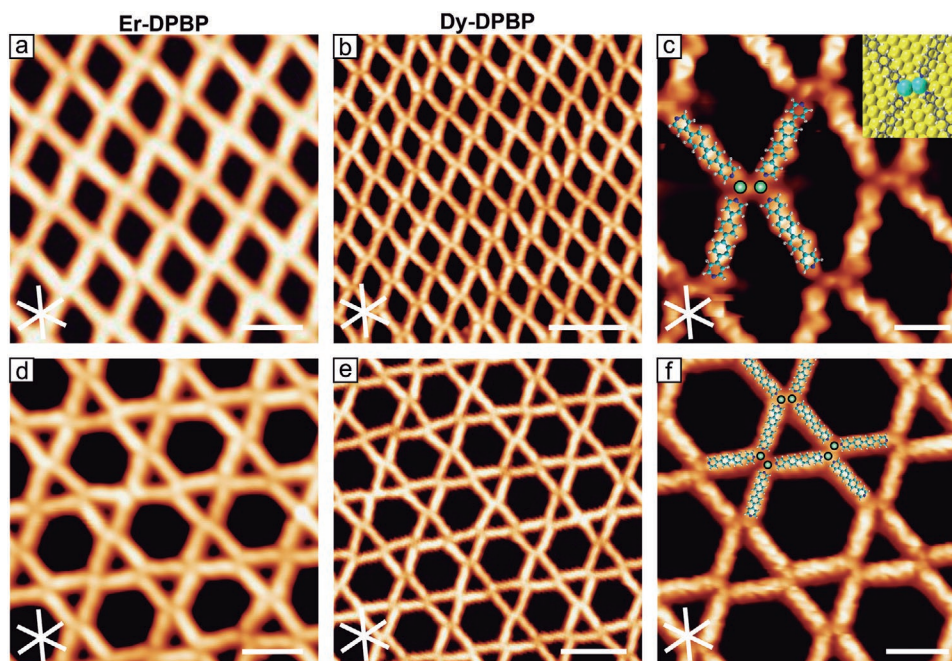


Figure 1. Er- and Dy-DPBP metallosupramolecular architectures on Au(111). a,b) STM images of rhombic Er- and Dy-DPBP networks, respectively. c) High-resolution STM image of rhombic Dy-DPBP network taken with a CO functionalized tip and the corresponding atomistic model. Green circles represent Dy atoms. White, cyan, and dark blue balls depict the H, C, and N atoms, respectively. The inset shows a top pictorial view of the DFT-based optimized rhombic Dy-DPBP network. d,e) STM images of Kagome Er- and Dy-DPBP networks, respectively. f) High-resolution STM image of the Kagome Dy-DPBP network taken with a CO functionalized tip, with an atomistic model superimposed. Scanning parameters: a) $V_b = 0.50$ V and $I_t = 100$ pA, b) $V_b = -1.00$ V and $I_t = 50$ pA, c) $V_b = 0.005$ V and $I_t = 50$ pA, d) $V_b = 0.50$ V and $I_t = 200$ pA, e) $V_b = -0.30$ V and $I_t = 200$ pA, f) $V_b = -0.10$ V and $I_t = 1500$ pA. Scale bars: a,d) 3 nm, b,e) 4 nm, c) 1 nm, and f) 2 nm.

Next, we have inspected the electronic properties of Er and Dy-DPBP networks. To this aim, we have first focused on the rhombic networks and performed STS at selected points on the substrate, metal centers, and linkers. As illustrated in **Figure 2a** for the rhombic Er-DPBP network, at negative bias voltages (occupied density of states) no resonance related to the assembly was detected within this voltage range. For positive bias voltages, probing the unoccupied density of states, a clear resonance at 1.78 V was observed on the ligand (grey line), tentatively assigned to the lowest unoccupied molecular orbital (LUMO). The nodes also feature a broad peak at 2.52 V. To assess the distribution over the network of the electronic density of such states, dI/dV mapping was performed at selected bias voltages (Figure 2c). At 1.78 V, it is manifested that the LUMO of the ligand is located on the pyridyl units, visualized as two bright lobes, one at each molecular termini. In addition, at 2.52 V the bimetallic node is seen as two bright protrusions decaying away into the molecular ligands, being such state assigned to the metallic centers.

Remarkably, analogous experiments on the rhombic Dy-DPBP network reveal a very similar electronic structure, just featuring a small shift towards Fermi energy of the resonances associated to the molecule and to the metal center of 0.29 V and 0.51 V, respectively (cf. bottom panel of Figure 2a and associated dI/dV maps). Such shift is well reproduced by the DFT simulations in the Projected Density of States (PDOS) profiles as shown in Figure S4 (Supporting Information), confirming our rationalization of the electronic structure of both Er-DPBP and Dy-DPBP networks.

In addition, we have explored the electronic properties of the Kagome Er- and Dy-DPBP networks. As illustrated in the STS of Figure 2b and associated dI/dV maps in Figure 2d, the Er- and Dy-directed assemblies display similar energy alignment of unoccupied frontier orbitals as their rhombic counterparts. The Kagome Dy-DPBP network also shows a shift of the states as compared to the Kagome Er case (see bottom part of Figure 2b).

Thus, it is feasible to tune the energy level alignment of the orbitals of the networks, while preserving the structure, by simply metal exchange, which heralds avenues for tailoring injection barriers for potential applications in organic optoelectronics and spintronics.

Subsequently, the magnetic properties of rhombic Er- and Dy-DPBP networks were investigated by XAS/XMCD/XLD. The quality of the networks was inspected by STM prior to beam exposure. **Figure 3a,b** presents experimental and simulated XAS and XMCD spectra for Er centers of the rhombic Er-DPBP network for both normal (NI – 0°) and grazing (GI – 70°) incidences. XAS spectra are characteristic of Er⁺³, featuring the second peak of the M₅-edge the most intense.^[37] XMCD spectra for NI and GI are almost identical with a slightly larger signal at normal incidence. Magnetization curves for both incidences are also very similar (Figure 3c). However, the curve at GI incidence seems to be more squared, indicating an easy axis of magnetization closer to the surface plane. In order to confirm the anisotropy orientation, additional field-dependent XMCD measurements were performed in the range of 1 T to –1 T and are presented as an inset in Figure 3c. The higher slope of the XMCD versus field curve at GI also indicates that the anisotropy

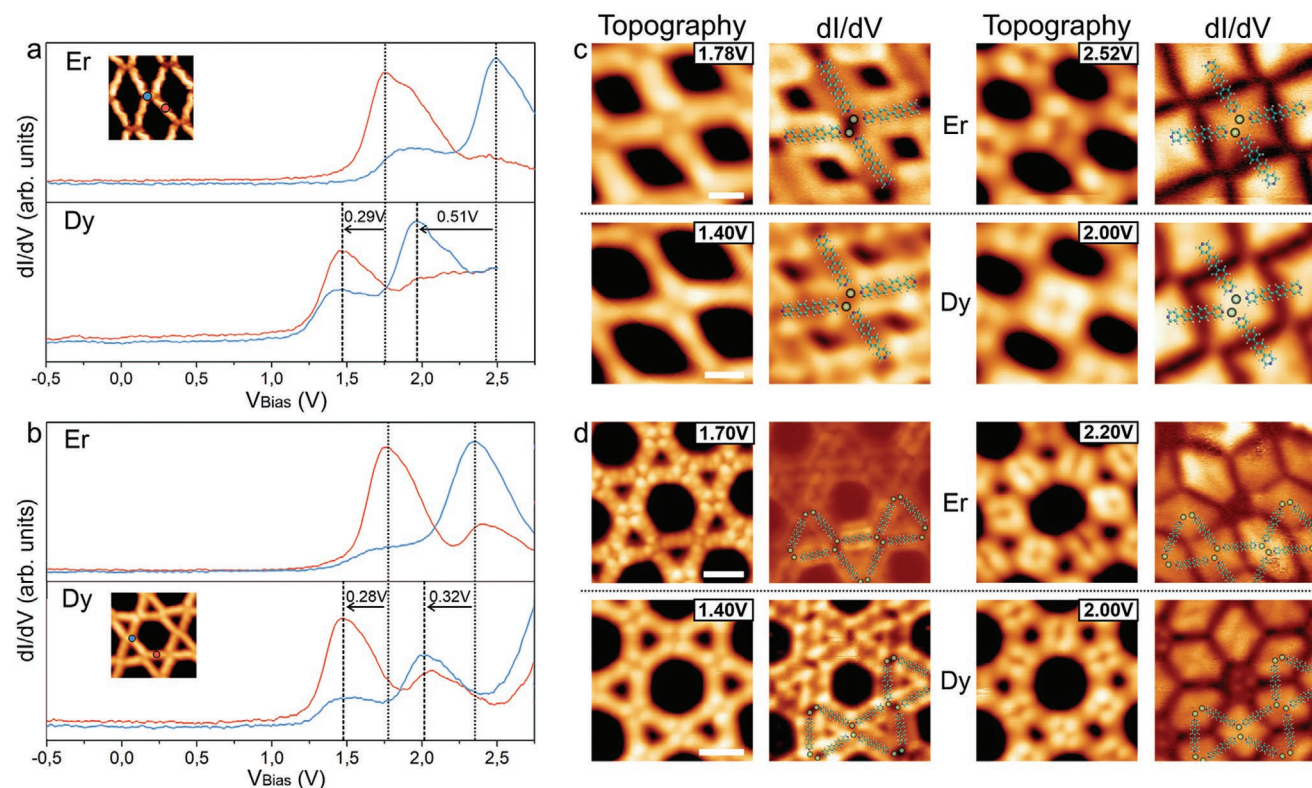


Figure 2. Electronic structure of Er- and Dy-DPBP rhombic and Kagome networks on Au(111). a) STS on Er- (upper panel) and Dy-directed rhombic networks (lower panel). b) STS on Er- (upper panel) and Dy-directed Kagome networks (lower panel). The spectra correspond to a metallic node (blue) and to the geometric center of DPBP species (red). The insets are high-resolution STM images of an Er-directed rhombic network (upper panel) and a Dy-directed Kagome network (lower panel), with blue and red circles displaying the positions of acquisition of STS. The dashed lines highlight the energy shift between Er and Dy networks. c) Topography and dI/dV maps of the corresponding states of the Er- and Dy-directed rhombic networks. An atomistic model is superimposed on the maps. d) Topography and dI/dV maps of the corresponding states of the Er- and Dy-directed Kagome networks with atomistic models superimposed on the maps. Scanning parameters: c) Upper left: $V_b = 1.78$ V and $I_t = 100$ pA, Upper right: $V_b = 2.52$ V and $I_t = 100$ pA, Lower left: $V_b = 1.40$ V and $I_t = 50$ pA, Lower right: $V_b = 2.00$ V and $I_t = 50$ pA; d) Upper left: $V_b = 1.60$ V and $I_t = 150$ pA, Upper right: $V_b = 2.20$ V and $I_t = 150$ pA, Lower left: $V_b = 1.40$ V and $I_t = 200$ pA, Lower right: $V_b = 2.00$ V and $I_t = 200$ pA. Scale bars: c) 1 nm, d) 2 nm.

axis is closer to the surface plane. Sum rules^[38,39] were used to extract the expectation values of spin ($\langle S_z \rangle$), orbital ($\langle L_z \rangle$), and total ($\langle J_z \rangle$) moments, as well as the total magnetic moment (M_T ; see Table 1). The smaller magnetic moments at GI when compared to the values at NI are within the experimental error, but could be attributed to an incomplete saturation of the sample. The XMCD measurement is an average of the different supramolecular domains displayed by Er-DPBP networks on Au(111), as typically encountered for metallosupramolecular architectures on surfaces. As a result, it is not feasible to achieve a complete saturation at GI in our experimental conditions.

A series of multiplet calculations using the MultiX code^[40] were performed in order to achieve a deeper understanding of the magnetic behavior of Er-DPBP networks (see Figures S5 and S6, Supporting Information). The simulated XAS/XMCD curves are presented together with the experimental data and display an excellent agreement, with both the peaks structure and intensity being successfully reproduced (see left panels of Figure 3; Figure S6, Supporting Information). Taking into account the existence of metallosupramolecular domains in the sample, the GI spectra were simulated by an azimuthal average of different in-plane orientations. These simulations indicate that there is a strong azimuthal anisotropy of the XMCD

intensity (see Figure S5, Supporting Information) and thus the experimentally observed similar intensity of the XMCD at GI is the result of the azimuthal average of domains with different orientations. Moreover, simulations of the polar angular dependence of the XMCD signal indicates that the magnetization presents a tilted easy axis, which is oriented at 50° with respect to the surface normal (see Figure S8, Supporting Information), being slightly closer to the surface plane, in agreement with the magnetization curves described above. These results are consistent with the recently reported magnetic behavior of dinuclear Er atoms,^[13,41] whose easy axis was located in the transition between in-plane and out-of-plane.

Furthermore, XAS/XMCD/XLD experiments were performed for the rhombic Dy-DPBP network to investigate the effect of metal exchange on the magnetic properties, while maintaining the same structural environment. XAS spectra (Figure 3e) also indicate a +3 oxidation state. Nevertheless, in this case, the system presents a high in-plane anisotropy, clearly observable in the XMCD spectra and magnetization curves (Figure 3f,g), demonstrating that it is possible to tune the easy axis of magnetization, while preserving the network structural integrity. In addition, the multiplet calculations match very well to the experimental data, reproducing the peaks structure

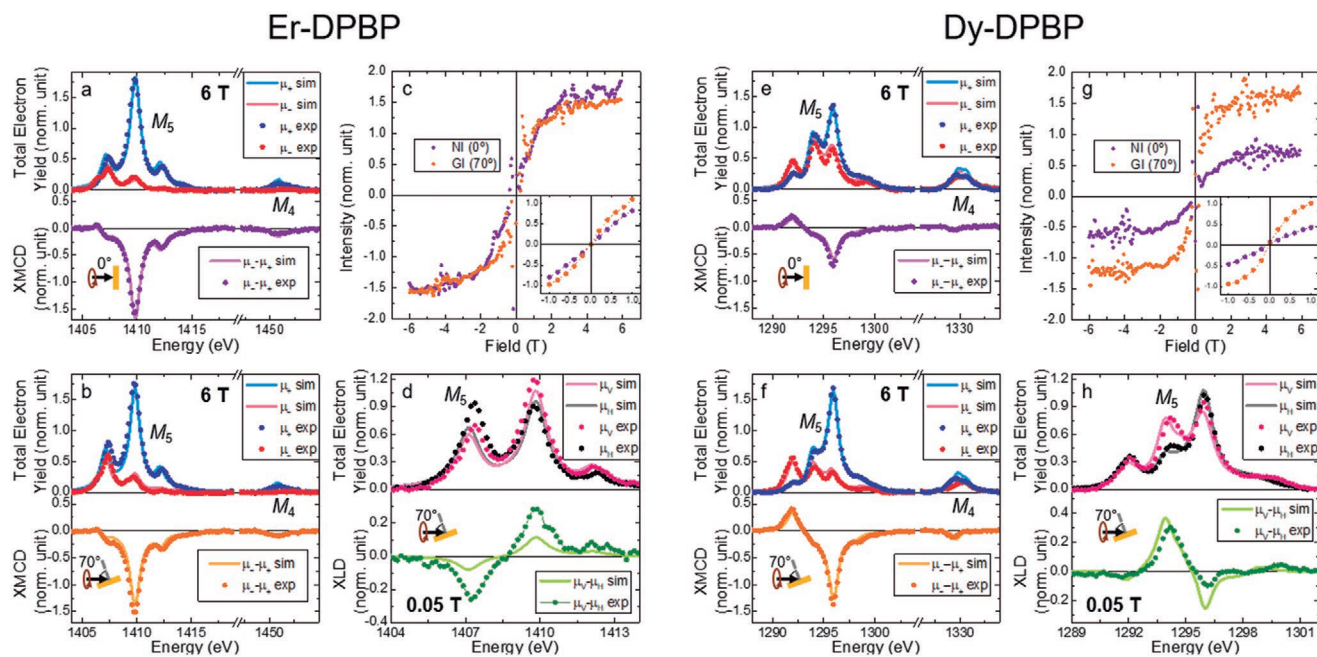


Figure 3. Magnetic structure of Er- and Dy-DPBP rhombic networks on Au(111). a–d) Er-DPBP; e–h) Dy-DPBP. a,b,e,f) XAS with positive (μ_+ , blue) and negative (μ_- , red) circularly polarized light and XMCD ($\mu_- - \mu_+$) taken at the Er/Dy $M_{4,5}$ -edges at a,e) normal (0° , purple) and b,f) grazing (70° , orange) incidences ($B = 6$ T, $T = 1.6$ K). c,g) Magnetization curves constructed by measuring the XMCD intensity at the most intense peak of the M_5 -edge. The inset shows field dependent measurements of XMCD intensity for fields ranging from 1 T to -1 T ($T = 1.6$ K). d,h) XAS spectra acquired with vertical (μ_v , pink) and horizontal (μ_h , black) linearly polarized light and XLD ($\mu_v - \mu_h$, green) taken at the Er/Dy M_5 -edge at grazing (70°) incidence ($B = 0.05$ T, $T = 1.6$ K).

and intensity (see Figure S7, Supporting Information). Finally, simulations of the polar angular dependence indicate that for Dy-DPBP the magnetic anisotropy axis is very close to the surface plane (80° with respect to the surface normal, see Figure S8, Supporting Information). These results are reinforced by experimental data of the polar angle dependence of XMCD of Dy-DPBP networks, which is in agreement with theoretical simulations including azimuthal averaging (see Figure S9, Supporting Information).

Expectation values of $\langle S_z \rangle$, $\langle L_z \rangle$, $\langle J_z \rangle$, and M_T for Dy centers of the rhombic Dy-DPBP network are presented in Table 1. As discussed for Er, the supramolecular orientational domains do not allow a full saturation and the values calculated by sum rules are lower limits for the saturation magnetic moments. These limit values imply that Er should have $J_z = 11/2$ or higher and Dy should have $J_z = 13/2$ or higher. According to the

Table 1. Expectation values of spin ($\langle S_z \rangle$), orbital ($\langle L_z \rangle$) and total ($\langle J_z \rangle = \langle S_z \rangle + \langle L_z \rangle$) moments, and total magnetic moment ($M_T = 2\langle S_z \rangle + \langle L_z \rangle$) extracted by XMCD sum rules for normal (0°) and grazing (70°) incidences for Er and Dy centers on the rhombic Er-DPBP and Dy-DPBP networks on Au(111).

Incidence angle [°]	Er centers on DPBP		Dy centers on DPBP	
	0 (NI)	70 (GI)	0	70
$\langle S_z \rangle$ (\hbar)	1.00(10)	0.95(10)	0.99(10)	1.99(20)
$\langle L_z \rangle$ (\hbar)	4.69(47)	3.89(39)	1.91(19)	4.46(45)
$\langle J_z \rangle$ (\hbar)	5.69(57)	4.84(48)	2.90(29)	6.45(64)
M_T (μ_B)	6.70(67)	5.79(58)	3.88(39)	8.44(84)

multiplet calculations, the values are $J_z = 15/2$ for both Er- and Dy-DPBP networks, and the lower experimental values are due to the azimuthal averaging of different domains. Notably, our multiplet simulations reveal that the magnetic anisotropy in Dy-DPBP is 2.6 times greater than in Er-DPBP (see Discussion in Supporting Information).

Finally, it is worth pointing out that in a general simplification about the electronic and magnetic properties of lanthanides, any hybridization of the 4f orbitals with the environment is neglected and the magnetic moments are closely related to the charge distribution of the 4f electrons.^[32,33] Such charge distribution will adapt to face the interactions with the crystal field, trying to diminish electrostatic repulsion, and thus stabilizing one of the allowed J_z quantum numbers for each specific coordination environment. Following this assumption, it should be expected that Er^{+3} would have a prolate charge density for large J_z , whereas Dy^{+3} would display an oblate charge density for high values of J_z .^[13,41] In the rhombic Er- and Dy-DPBP networks, the coordination symmetry is the same. However, the XLD measurements, which peak orientation is well reproduced by the simulations (see Figure 3d–h), indicate that the charge densities of the metallic centers are inverted. These distributions of the charge together with the expression of high magnetic moments can be rationalized within such general simplification picture of the relationship between charge and magnetic moment. Following this assumption, for Dy^{+3} , the oblate charge would be out-of-plane with a high in-plane magnetic moment, whereas for Er^{+3} the prolate charge would be closer to the plane than to the normal, in a tilted fashion following the anisotropy orientation, as well as the high magnetic moment.

In a recent work, we have demonstrated that the anisotropy of lanthanide systems is very complex, with the coordination symmetry and the interaction with the charges of the crystal field playing decisive roles.^[42] As a result, minute differences in the distribution of the charge imply critical changes in the resulting magnetic anisotropy. Consequently, for the more out-of-plane oblate charge density of Dy⁺³ the magnetic anisotropy is in-plane, whereas for the prolate density of Er⁺³ the easy axis assumes a tilted orientation.

3. Conclusion

In summary, we describe the on-surface synthesis of lanthanide-directed porous networks based on dinuclear nodes. Two distinct architectures could be achieved by controlling the molecular and lanthanide coverage on the surface, i.e., rhombic and Kagome networks. Importantly, such architectures based either on Er or Dy display the same network structure.

Despite presenting identical +3 oxidation state and structure, the experimental fingerprints of the unoccupied density of states reveal a shift between the Er- and Dy-directed networks, thus anticipating fascinating ways to engineer the energy level alignment of lanthanide-directed networks, while preserving the structure. In addition, the inspection and rationalization of the magnetic properties show that it is feasible to tailor both the orientation of the easy axis of magnetization and the magnetic anisotropy, while exchanging the lanthanide metal, i.e., moving from Er to Dy.

Our study opens avenues to design bi-dimensional metal-organic materials that keep the same structure, but allow tunable energy level alignment and magnetic anisotropy by metal exchange. Taking into account that the family of lanthanides is formed by 14 elements, our discovery reveals pathways for regulating the functional properties of lanthanide-directed nanomaterials.

4. Experimental Section

IMDEA Nanoscience: The scanning tunnelling microscopy (STM) and scanning tunnelling spectroscopy (STS) experiments were performed in IMDEA Nanoscience in an ultra-high vacuum (UHV) setup with a base pressure of 1×10^{-10} mbar, hosting a commercial low-temperature STM from Omicron held at cryogenic temperatures (4.3 K). The images have been taken in constant current mode, with a bias voltage (V_b) applied to the sample, employing electrochemically etched Au tips. dI/dV curves were recorded with the feedback loop opened, and dI/dV maps with a closed feedback loop, both using the lock-in technique (SRS830) with a typical modulation voltage of 20 mV_{rms}.

Prior to start the experiments, the Au(111) crystal was prepared by repeated cycles of standard Ar⁺ sputtering (1.5 keV, 10 μ A, 10 min) and subsequent annealing to 723 K during 10 min. Then, the DPBP species were deposited on top of the pristine substrate by molecular beam epitaxy from a quartz crucible held at 410 K (Kentax TCE-BSC). Molecular flux was checked with a quartz crystal microbalance (LewVac). Er/Dy atoms were deposited from a Focus EFM3Ts evaporator using degassed Er/Dy rods. During this stage of the growth, the substrate was held at room temperature (300 K). Finally, the samples were annealed to 425 K during 30 min.

Atomistic models employed in this work were obtained by optimizing the DPBP structure in gas phase in the HyperChem software package^[43] (MM+ method) and superimposing it on the calibrated STM images. The intermetallic distances (Er–Er and Dy–Dy) and the bond length between

the pyridyl groups and the metallic centers were obtained from these models by measuring: i) the projected distances between centers of metallic atoms in the same node, and ii) the distances from the center of the metallic atom and the terminal nitrogen of the surrounding ligands.

ALBA Synchrotron: The samples were prepared following the same procedures described in the previous section, in a UHV set-up located at ALBA synchrotron with base pressure below 5×10^{-10} mbar. For synchrotron samples, special care was taken with respect to the proportion of molecules/metal in the samples. They were prepared with an excess of molecules in order to guarantee that all metallic atoms were coordinated. This ensures that the magnetic signal was generated integrally by coordinated metallic centers. After the sample preparation, the morphology of the networks was checked with an RHK Pan Flow STM operating at liquid nitrogen temperatures using electrochemically etched W tips.

X-ray absorption spectroscopy (XAS), X-ray magnetic circular dichroism (XMCD), and X-ray linear dichroism (XLD) experiments were done at BOREAS beamline of ALBA synchrotron light source, Spain.^[44] The measurements were performed with a 90% circularly polarized beam in total electron yield (TEY) mode at a nominal temperature of 1.6 K. Absorption spectra with circular polarizations were taken at Er (Dy) M_{4,5}-edges at fields of 6 T with normal (NI, 0°) and grazing (GI, 70°) incidences. XMCD is the difference between spectra with negative and positive polarizations ($\mu_L - \mu_H$). The spectra were normalized to the maximum in the M₅-edge of the average absorption spectra, $Ave_{XAS} = \left(\frac{\mu_+ + \mu_-}{2} \right)$. Absorption spectra with linear polarizations were taken at Dy and Er M₅-edges at fields of 0.05 T at GI. XLD is the difference between spectra with vertical and horizontal polarizations ($\mu_V - \mu_H$). The spectra were normalized to the maximum in the M₅-edge of the isotropic absorption spectra, $Iso_{XLD} = \left(\frac{1}{3} \mu_V + \frac{2}{3} \mu_H \right)$.

Expectation values of the orbital moment $\langle L_z \rangle$ and effective spin moment $\langle S_z^{eff} \rangle$ in units of \hbar were calculated using sum rules^[38,39] with a number of holes equal to 3 for Er⁺³ and 5 for Dy⁺³. The expectation values of the spin moment $\langle S_z \rangle$ in units of \hbar were determined by the relation $\langle S_z^{eff} \rangle = \langle S_z \rangle + 3 \langle T_z \rangle$, and assuming that the ratio $\langle T_z \rangle / \langle S_z \rangle$ was constant and equal to -0.053 for Dy⁺³ and $+0.213$ for Er⁺³.^[45] The expectation values of the total moment $\langle J_z \rangle = \langle S_z \rangle + \langle L_z \rangle$ in units of \hbar , and $M_T = 2 \langle S_z \rangle + \langle L_z \rangle$ in μ_B were also calculated.

It is important to point out that the calculated expectation values were the projection of the magnetic moments at the direction of the X-ray incidence at the experimental conditions of 6 T and 1.6 K and represent lower limits to the real values of the magnetic moments. As the sample was composed by supramolecular domains with six possible orientations, what was measured was an average of these domains and it was not possible to achieve a full saturation at the surface plane. This effect was especially relevant for samples with in-plane anisotropy.

Despite the Ln–Ln distance was short enough for establishing magnetic exchange interactions, neither STS nor XMCD detected any fingerprint of them.

Theoretical Methods: Density Functional Theory: The first-principles atomistic simulations of the two rhombic Dy- and Er-DPBP networks, to compute optimized interfacial structures and electronic properties, had been performed by DFT as implemented in the plane-wave QUANTUM ESPRESSO simulation package.^[46] One-electron wave-functions were expanded in a plane-waves basis with energy cutoffs of 550 and 650 eV for the kinetic energy and the electronic density, respectively. Exchange and correlation had been computed in the revised generalized gradient corrected approximation PBESol.^[47,48] Kresse-Joubert projector augmented wave pseudopotentials^[49] were adopted to model the ion-electron interaction for all the involved atoms (H, C, N, Dy, Er, and Au). Besides, 20 and 22 valence electrons were accounted for the Dy and Er atoms, respectively, to include the role of the lanthanide 4f¹⁰ electrons in the subtle interfacial chemistry. These numerical implementations were necessary to obtain binuclear nodes Dy–Dy and Er–Er within the networks with distances consistent with the experimental results. In all the calculations Brillouin zones were sampled using optimal ($2 \times 2 \times 1$) Monkhorst-Pack grids.^[50] A perturbative van der Waals (vdW) correction, with an empirical vdW-R⁻⁶ correction, was used to add dispersive forces

to the conventional density functional (DFT+D3).^[51] All the calculations were performed by considering spin-polarization. Atomic relaxations were carried out using a conjugate gradient minimization scheme until the maximum force on any atom was lower than 0.02 eV Å⁻¹. The Fermi level was smeared out using the Methfessel-Paxton approach^[52] with a Gaussian width of 0.01 eV, and all energies were extrapolated to $T = 0$ K. Self-consistency in the electron density was converged to a precision in the total energy better than 10⁻⁶ eV.

Theoretical Methods: Multiplet Calculations: XAS, XMCD, and XLD spectra of Er- and Dy-DPBP networks have been simulated by means of multiplet calculations using the code MultiX.^[40] Er³⁺ and Dy³⁺ ions were simulated with 3d¹⁰4f¹¹ and 3d¹⁰4f⁹ ground states, respectively. The Hartree–Fock parameters for Er (Dy) were rescaled by factors of 0.98 (0.98) for the spin-orbit coupling and 0.93 (0.80) for the Coulomb interaction and a core–hole broadening of 0.55 eV (0.50 eV) was used to reproduce the experimental resolution.

MultiX used a point charge model where the crystal field (CF) acting in the magnetic center was simulated by the interaction of surrounding atoms by indicating their coordinates and charges. DFT data was used as a reference for the CF modeling and the charges were adjusted to fit the simulations to the experimental data. The code only allows the simulation of one magnetic atom and the second metallic center of the binuclear nodes was simulated as a point charge with the same +3 charge as the magnetic one.

Supporting Information

Supporting Information is available from the Wiley Online Library or from the author.

Acknowledgements

D.M. and S.O.P. contributed equally to this work. The ALBA synchrotron was acknowledged for providing beam time at BOREAS beamline (proposal numbers 2020024200 and 2020094657). This project had received funding from the European Research Council (ERC, grant 766555) and Marie Skłodowska-Curie Actions (MSCA, project 894924) under the European Union's Horizon 2020 research and innovation programme. IMDEA Nanociencia acknowledges support from the “Severo Ochoa” Programme for Centres of Excellence in R&D (MINECO, Grant SEV-2016-0686).

Conflict of Interest

The authors declare no conflict of interest.

Data Availability Statement

The data that support the findings of this study are available from the corresponding author upon reasonable request.

Keywords

lanthanides, magnetic anisotropy, metal exchange, metal-organic networks, scanning tunneling microscopy, X-ray magnetic circular dichroism

Received: November 16, 2021
Revised: February 16, 2022
Published online: April 8, 2022

- [1] J.-C. G. Bünzli, *Acc. Chem. Res.* **2006**, *39*, 53.
- [2] S. V. Eliseeva, J.-C. G. Bünzli, *New J. Chem.* **2011**, *35*, 1165.
- [3] J.-C. G. Bünzli, *J. Coord. Chem.* **2014**, *67*, 3706.
- [4] S. V. Eliseeva, J.-C. G. Bünzli, *Chem. Soc. Rev.* **2010**, *39*, 189.
- [5] D. N. Woodruff, R. E. P. Winpenny, R. A. Layfield, *Chem. Rev.* **2013**, *113*, 5110.
- [6] A. Gaita-Arino, H. Prima-Garcia, S. Cardona-Serra, L. Escalera-Moreno, L. E. Rosaleny, J. J. Baldovi, *Inorg. Chem. Front.* **2016**, *3*, 568.
- [7] R. Vincent, S. Klyatskaya, M. Ruben, W. Wernsdorfer, F. Balestro, *Nature* **2012**, *488*, 357.
- [8] S. Thiele, F. Balestro, R. Ballou, S. Klyatskaya, M. Ruben, W. Wernsdorfer, *Science* **2014**, *344*, 1135.
- [9] G. Aromí, F. Luis, O. Roubeau, in *Lanthanides and Actinides in Molecular Magnetism*, Wiley-VCH, **2015**, Ch. 7.
- [10] F. Donati, S. Rusponi, S. Stepanow, C. Wäckerlin, A. Singha, L. Persichetti, R. Baltic, K. Diller, F. Patthey, E. Fernandes, J. Dreiser, Ž. Šljivančanin, K. Kummer, C. Nistor, P. Gambardella, H. Brune, *Science* **2016**, *352*, 318.
- [11] F. D. Natterer, K. Yang, W. Paul, P. Willke, T. Choi, T. Greber, A. J. Heinrich, C. P. Lutz, *Nature* **2017**, *543*, 226.
- [12] S. T. Liddle, J. van Slageren, *Chem. Soc. Rev.* **2015**, *44*, 6655.
- [13] J. D. Rinehart, J. R. Long, *Chem. Sci.* **2011**, *2*, 2078.
- [14] C. Wäckerlin, F. Donati, A. Singha, R. Baltic, S. Rusponi, K. Diller, F. Patthey, M. Pivetta, Y. Lan, S. Klyatskaya, M. Ruben, H. Brune, J. Dreiser, *Adv. Mater.* **2016**, *28*, 5195.
- [15] L. Margheriti, D. Chiappe, M. Mannini, P.-E. Car, P. Saintavitt, M.-A. Arrio, F. B. de Mongeot, J. C. Cezar, F. M. Piras, A. Magnani, E. Otero, A. Caneschi, R. Sessoli, *Adv. Mater.* **2010**, *22*, 5488.
- [16] N. Ishikawa, Y. Mizuno, S. Takamatsu, T. Ishikawa, S. Koshihara, *Inorg. Chem.* **2008**, *47*, 10217.
- [17] P. Zhang, L. Zhanga, J. Tang, *Dalton Trans.* **2015**, *44*, 3923.
- [18] R. J. Blagg, L. Ungur, F. Tuna, J. Speak, P. Comar, D. Collison, W. Wernsdorfer, E. J. L. McInnes, L. F. Chibotaru, R. E. P. Winpenny, *Nat. Chem.* **2013**, *5*, 673.
- [19] R. Marin, G. Brunet, M. Murugesu, *Angew. Chem., Int. Ed.* **2021**, *60*, 1728.
- [20] J. Jiang, Y. Zhao, O. M. Yaghi, *J. Am. Chem. Soc.* **2016**, *138*, 3255.
- [21] A. E. Thorarindottir, T. D. Harris, *Chem. Rev.* **2020**, *120*, 8716.
- [22] L. S. Xie, G. Skorupskii, M. Dincă, *Chem. Rev.* **2020**, *120*, 8536.
- [23] J. V. Barth, G. Costantini, K. Kern, *Nature* **2005**, *437*, 671.
- [24] J. V. Barth, *Annu. Rev. Phys. Chem.* **2007**, *58*, 375.
- [25] L. Dong, Z. A. Gao, N. Lin, *Prog. Surf. Sci.* **2016**, *91*, 101.
- [26] D. Ćcija, J. I. Urgel, A. P. Seitsonen, W. Auwärter, J. V. Barth, *Acc. Chem. Res.* **2018**, *51*, 365.
- [27] D. Ćcija, J. I. Urgel, A. C. Papageorgiou, S. Joshi, W. Auwärter, A. P. Seitsonen, S. Klyatskaya, M. Ruben, S. Fischer, S. Vijayaraghavan, J. Reichert, J. V. Barth, *Proc. Natl. Acad. Sci. USA* **2013**, *110*, 6678.
- [28] J. I. Urgel, B. Cirera, Y. Wang, W. Auwärter, R. Otero, J. M. Gallego, M. Alcamí, S. Klyatskaya, M. Ruben, F. Martin, R. Miranda, D. Ćcija, J. V. Barth, *Small* **2015**, *47*, 6358.
- [29] J. I. Urgel, D. Ćcija, W. Auwärter, D. Stassen, D. Bonifazi, J. V. Barth, *Angew. Chem., Int. Ed.* **2015**, *54*, 6163.
- [30] B. Cirera, L. Dordevic, R. Otero, J. M. Gallego, D. Bonifazi, R. Miranda, D. Ćcija, *Chem. Commun.* **2016**, *52*, 11227.
- [31] G. Lyu, Q. Zhang, J. I. Urgel, G. Kuang, W. Auwärter, D. Ćcija, J. V. Barth, N. Lin, *Chem. Commun.* **2016**, *52*, 1618.
- [32] M. Uphoff, G. S. Michelitsch, R. Hellwig, K. Reuter, H. Brune, F. Klappenberger, J. V. Barth, *ACS Nano* **2018**, *12*, 11552.
- [33] D. Moreno, B. Cirera, S. O. Parreiras, J. I. Urgel, N. Giménez-Agulló, K. Lauwaet, J. M. Gallego, J. R. Galán-Mascarós, J. I. Martínez, P. Ballester, R. Miranda, D. Ćcija, *Chem. Commun.* **2021**, *57*, 1380.
- [34] J. Liu, J. Li, Z. Xu, X. Zhou, Q. Xue, T. Wu, M. Zhong, R. Li, R. Sun, Z. Shen, H. Tang, S. Gao, B. Wang, S. Hou, Y. Wang, *Nat. Commun.* **2021**, *12*, 1619.

- [35] F. Klappenberger, *Prog. Surf. Sci.* **2014**, *89*, 1.
- [36] A. Singha, R. Baltic, F. Donati, C. Wäckerlin, J. Dreiser, L. Persichetti, S. Stepanow, P. Gambardella, S. Rusponi, H. Brune, *Phys. Rev. B* **2017**, *96*, 224418.
- [37] B. T. Thole, P. Carra, F. Sette, G. van der Laan, *Phys. Rev. Lett.* **1992**, *68*, 1943.
- [38] P. Carra, B. T. Thole, M. Altarelli, X. Wang, *Phys. Rev. Lett.* **1993**, *70*, 694.
- [39] A. Uldry, F. Vernay, B. Delley, *Phys. Rev. B* **2012**, *85*, 125133.
- [40] A. Singha, F. Donati, C. Wäckerlin, R. Baltic, J. Dreiser, M. Pivetta, S. Rusponi, H. Brune, *NanoLett.* **2016**, *16*, 3475.
- [41] S. O. Parreiras, D. Moreno, B. Cirera, M. A. Valbuena, J. I. Urgel, M. Paradinas, M. Panighel, F. Ajejas, M. A. Niño, J. M. Gallego, M. Valvidares, P. Gargiani, W. Kuch, J. I. Martínez, A. Mugarza, J. Camarero, R. Miranda, P. Perna, D. Écija, *Small* **2021**, *17*, 2102753.
- [42] HyperChem(TM) Professional 7.51, Hypercube, Inc., 1115 NW 4th Street, Gainesville, Florida 32601, USA.
- [43] A. Barla, J. Nicolas, D. Cocco, S. M. Valvidares, J. Herrero-Martin, P. Gargiani, J. Moldes, C. Ruget, E. Pellegrin, S. Ferrer, *J. Synchrotron Rad.* **2016**, *23*, 1507.
- [44] Y. Teramura, A. Tanaka, B. T. Thole, T. Jo, *J. Phys. Soc. Jpn.* **1996**, *65*, 3056.
- [45] P. Giannozzi, S. Baroni, N. Bonini, M. Calandra, R. Car, C. Cavazzoni, D. Ceresoli, G. L. Chiarotti, M. Cococcioni, I. Dabo, A. Dal Corso, S. de Gironcoli, S. Fabris, G. Fratesi, R. Gebauer, U. Gerstmann, C. Gougoussis, A. Kokalj, M. Lazzeri, L. Martin-Samos, N. Marzari, F. Mauri, R. Mazzarello, S. Paolini, A. Pasquarello, L. Paulatto, C. Sbraccia, S. Scandolo, G. Sclauzero, A. P. Seitsonen, et al., *J. Phys.: Condens. Matter* **2009**, *21*, 395502.
- [46] L. A. Constantin, J. P. Perdew, J. M. Pitarke, *Phys. Rev. B* **2009**, *79*, 075126.
- [47] J. P. Perdew, A. Ruzsinszky, G. I. Csonka, O. A. Vydrov, G. E. Scuseria, L. A. Constantin, X. Zhou, K. Burke, *Phys. Rev. Lett.* **2008**, *100*, 136406.
- [48] G. Kresse, J. Joubert, *Phys. Rev. B* **1999**, *59*, 1758.
- [49] J. D. Pack, H. J. Monkhorst, *Phys. Rev. B* **1977**, *16*, 1748.
- [50] S. Grimme, J. Antony, S. Ehrlich, H. Krieg, *J. Chem. Phys.* **2010**, *132*, 154104.
- [51] M. Methfessel, A. T. Paxton, *Phys. Rev. B* **1989**, *40*, 3616.